Injection-molded lenses have an inhomogeneous stress-induced birefringence that can degrade optical performance. To address this issue, numerous studies have been conducted to investigate the residual stress and resulting birefringence caused by molding conditions [1, 2]. In our research, a tomographic reconstruction of a 3D birefringence distribution is sought from a linear line projection relationship between the spatially varying index ellipsoids and polarimetric observations. This paper is divided into three sections: "Optical Physics", "Optical Engineering", and "Image Science". In the first section "Optical Physics", the concept of birefringence and the properties of a light source are discussed. Here, the definition of birefringence is provided, which states that the value of birefringence relative to the orientation of the polarization can be determined from Maxwell's equations, introducing a dielectric tensor and an index ellipsoid. In the second section "Optical Engineering", a commercially available 2D birefringence analyzer is explained, with a focus on the polarimeter components [3]. In the last section "Image Science", tomographic reconstruction algorithms are reconciled with 3D birefringence distribution definitions.

1 Background (Optical Physics)

1.1 Stress-induced birefringence

An index ellipsoid is used to define the polarization-dependent refractive index (i.e. birefringence) of a material. This section explains the concept of birefringence for transmitted light, based on the index ellipsoid.

1.1.1 Dielectric tensor Assuming that no source resides in free space, transforming Maxwell's equations into the Fourier domain, and combining the 2nd and 3rd equations (that is $\nabla \times \mathbf{H} = \partial \mathbf{D}/\partial t$ and $\nabla \times \mathbf{E} = -\partial \mathbf{B}/\partial t$) [4], the following formula can be obtained: $\mathbf{k} \times (\mathbf{k} \times \mathbf{E}) = -\omega^2 \, \mu_0 \, \mu(\omega) \, \mathbf{D}$. Here, ω is the light frequency, while μ_0 and $\mu(\omega)$ are the free space and material permeabilities, respectively. This equation states that the displacement field $\mathbf{D}$ and the wave vector $\mathbf{k}$ are always perpendicular, while $\mathbf{D}$ and the electric field $\mathbf{E}$

are not necessarily parallel. In an isotropic medium, $\mathbf{D}$ and $\mathbf{E}$ are always parallel since the relationship between them is expressed as $\mathbf{D} = \varepsilon_0\,\varepsilon(\omega)\,\mathbf{E}$ where ε_0 and $\varepsilon(\omega)$ are the free space and material permittivities, respectively. On the other hand, in an anisotropic medium where $\mathbf{D}$ and $\mathbf{E}$ are not necessarily parallel, the relationship between them can be given by $\mathbf{D} = \varepsilon_0\,\boldsymbol{\varepsilon}\,\mathbf{E}$ where $\boldsymbol{\varepsilon}$ is a 3×3 matrix referred to as a dielectric tensor [5], which works similarly to the material permittivity $\varepsilon(\omega)$ and can define a 3D refractive index. If the three principal axes are aligned with the (x, y, z) axes, the dielectric tensor is diagonal and $\mathbf{D}$ can be written as

$$
\begin{pmatrix} D_x \\ D_y \\ D_z \end{pmatrix} = \varepsilon_0 \begin{pmatrix} n_x^2 & 0 & 0 \\ 0 & n_y^2 & 0 \\ 0 & 0 & n_z^2 \end{pmatrix} \begin{pmatrix} E_x \\ E_y \\ E_z \end{pmatrix}. \tag{1}
$$

The dielectric tensor expressed in Equation 1 allows for the establishment of distinct refractive indices in each axis for an anisotropic material.

1.1.2 Index ellipsoid The energy density u of the electromagnetic wave is expressed as $u = \mathbf{E}\,\mathbf{D}/2$. By inserting Equation 1 into the energy density equation and taking into account that the inverse of the diagonal matrix $\boldsymbol{\varepsilon}$ is obtained by replacing each diagonal element with its reciprocal, the following is obtained

$$
\frac{(D_x/\sqrt{2\,u\,\varepsilon_0})^2}{n_x^2} + \frac{(D_y/\sqrt{2\,u\,\varepsilon_0})^2}{n_y^2} + \frac{(D_z/\sqrt{2\,u\,\varepsilon_0})^2}{n_z^2} = 1. \tag{2}
$$

Since u is constant, Equation 2 describes a 3D ellipsoid with (n_x, n_y, n_z) as its basis on the (x, y, z) axes, as illustrated in Figure 1a. This ellipsoid is referred to as an index ellipsoid [6], and the refractive index associated with a given $\mathbf{D}$ field can be calculated. There are no restrictions on which principal index is aligned with a particular basis dimension, thus allowing the ellipsoid to have three degrees of rotational freedom.

Figure 1b diagrams the process of transforming birefringence from a given index ellipsoid

(a) Index ellipsoid   **(b)** Birefringence
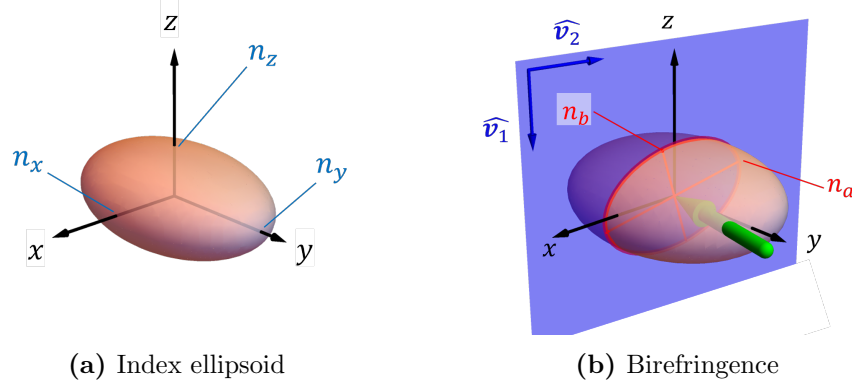
Figure 1: (a) The 3D index ellipsoid's geometry is determined by the refractive index magnitudes along each axis, n_x, n_y, and n_z. The term $(D_x, D_y, D_z)/\sqrt{2\,u\,\varepsilon_0}$ in Equation 2 is replaced by the (x, y, z) basis. (b) The birefringence of transmitted light is represented by a 2D cross-sectional red ellipse. The transverse plane (purple) is orthogonal to the wave vector $\mathbf{k}$ (green arrow) and contains the unit vectors $\widehat{\mathbf{v}_1}$, $\widehat{\mathbf{v}_2}$ and the origin. The birefringence for the transmitted light is defined by n_a and n_b, the major and minor axes of the cross-section.

and ray direction. The green arrow in the figure symbolizes the wave vector $\mathbf{k}$. As Section 1.1.1 explains, $\mathbf{k}$ and $\mathbf{D}$ are perpendicular, so the birefringence of the transmitted light is determined by a 2D cross-sectional red ellipse created by slicing the index ellipsoid. This 2D ellipse contains the transverse plane shown in purple, the unit vectors $\widehat{\mathbf{v}}_1$, $\widehat{\mathbf{v}}_2$, and the origin. The major and minor axes of the cross-sectional 2D ellipse are in red lines, and n_a and n_b represent the orthogonal birefringence values for the respective orientations.

1.1.3 Cross-sectional index ellipse The cross-section of the ellipsoid has been investigated using computational techniques by other authors [7, 8]. Here, the main points of these calculations are summarized. A 3D ellipsoid centered at the origin is given by $\mathbf{r}^T \mathbf{Q}\, \mathbf{r} = 1.$, where the six unique elements of the Hermitian 3×3 matrix $\mathbf{Q}$ determine the shape and principal axes of the ellipsoid, and the vector $\mathbf{r}$ gives the basis defined by $\mathbf{r} = (x, y, z)^T$. The matrix $\mathbf{Q}$ can be written as $\mathbf{U_Q}\mathbf{\Lambda_Q}\mathbf{U_Q}^T$. The diagonal elements of $\mathbf{\Lambda_Q}$ are $1/n_1^2$, $1/n_2^2$, and $1/n_3^2$, where n_1, n_2, and n_3 are the magnitudes of the ellipsoid along the principal axes. The singular vectors, which are columns of $\mathbf{U_Q}$, give the direction of the principal axes.

A 2D cross-sectional ellipse centered at the origin is represented by $\mathbf{P} = \mathbf{V}^T \mathbf{Q}\, \mathbf{V}$. The three unique elements of the Hermitian 2×2 matrix $\mathbf{P}$ determine the principal axes and

shape of the ellipse. The 3×2 matrix $\mathbf{V}$ is named a cross-sectional matrix, and the singular vectors $\widehat{\mathbf{v}}_i$ shown in Figure 1b are the columns of $\mathbf{V}$. Similarly, consider $\mathbf{P} = \mathbf{U_P} \mathbf{\Lambda_P} \mathbf{U_P}^T$. The two values $1/n_a{}^2$ and $1/n_b{}^2$ are the diagonal elements of $\mathbf{\Lambda_P}$, and n_a and n_b are the magnitudes of the ellipse seen in Figure 1b. The columns of $\mathbf{U_P}$ are unit vectors in the direction of the major and minor axes of the cross-sectional 2D ellipse.

1.2   Light source

The commercially available 2D birefringence analyzer, WPA-100, manufactured by Photonic Lattice is shown in Figure 2 [3]. The WPA-100 system utilizes white LEDs as its light source. The unpolarized light emitted from the LEDs is circularly polarized through a circular polarization filter and then illuminated onto an object. The transmitted light from the object is evaluated by a polarimeter, which computes a 2D birefringence distribution. This distribution has an angular dependence, so circularly polarized light, which can be decomposed into two orthogonal linear states with any orientation, is used to cover all directions. The polarimeter is also equipped with three different wavelength filters (523nm, 543nm, and 575nm) to calculate the 2D birefringence distribution for each wavelength. Generally, the maximum retardance a single wavelength can measure is $\lambda/2$, but by combining multi-wavelength measurements and employing curve-fitting algorithms [9, 10], the maximum measurable retardance can be increased. The WPA-100 system adopts these methods
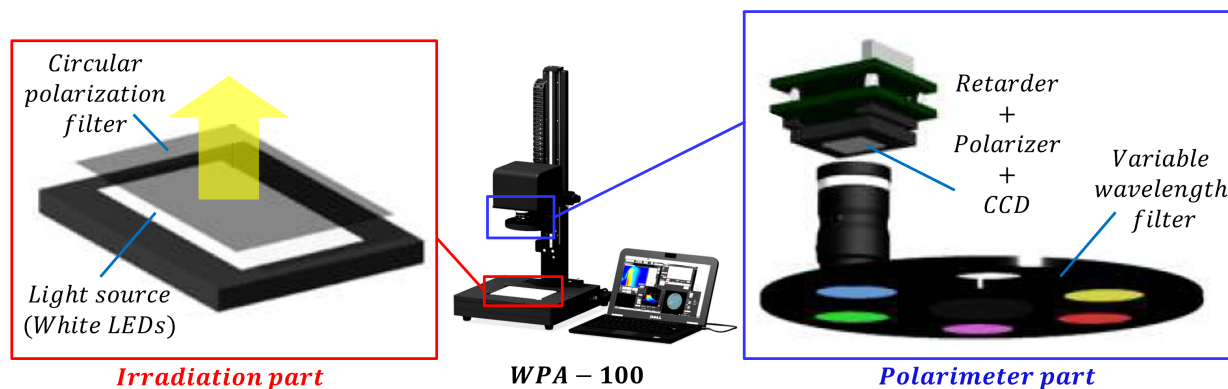
Figure 2: Birefringence analyzer WPA-100 produced by Photonic Lattice [3].

and can measure retardance up to 2λ. Since the system requires multiple wavelengths, a laser with a narrow wavelength bandwidth is not suitable as a light source; therefore, white LEDs are adopted.

2   Instrument (Optical Engineering)

2.1   2D Birefringence Analyzer

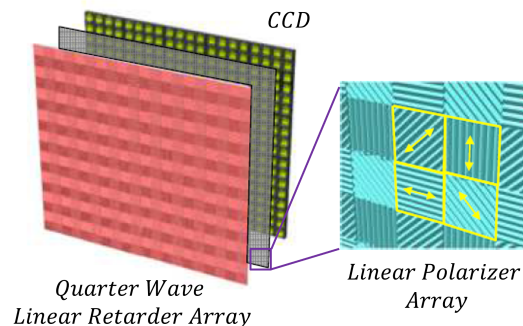As depicted in Figure 2, the polarimeter is composed of a retarder, polarizer, and CCD. Figure 3 provides more information about these components. All of them have an array structure and do not involve any mechanical movement, such as rotation. The polarizer array is made up of four micron-sized polarizers

Figure 3: The polarimeter is composed of a retarder, polarizer, and CCD [3]. All components have micro-sized array structures, and the retarder functions as a quarter-wave retarder for all arrays.

oriented at 0°, 45°, 90°, and 135°, which is not notable for its widespread usage. The retarder array is produced by the unique technology of Photonic Lattice. It also has an array structure and functions as a quarter-wave retarder for all arrays. The orientations of the fast axes can be determined for each array individually, but their directions are not revealed. Since it is known that full Stokes parameters can be obtained from these components, testing will be conducted to decide the appropriate orientations of the fast axes.
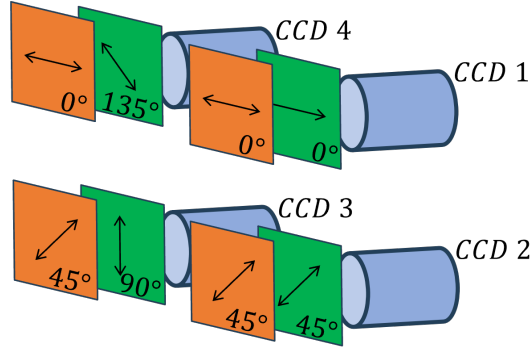
Consider the definition

$$\mathbf{J}_{out} = \mathbf{LP}(\theta_p) \, \mathbf{LR}(\delta, \theta_r) \, \mathbf{J}_{in} \tag{3}$$

Here, $\mathbf{J}_{in}$ and $\mathbf{J}_{out}$ denote the incident and outgoing Jones vectors, respectively. $\mathbf{LP}$ and $\mathbf{LR}$ stand for a linear polarizer and a linear retarder, and the variables of $\mathbf{LP}$ and $\mathbf{LR}$ are θ_p, the orientation of the transmission axis; δ, the retardance, which is set to $\lambda/4$ in this polarimeter; and θ_r, the orientation of the fast axis, whose values are not revealed for all arrays. Equation 3 can be used to calculate the Jones vectors for the polarimeter seen

Figure 4: Green and orange squares denote polarizers and retarders, respectively. Arrows on the polarizers indicate the transmission axes, whereas arrows on the retarders indicate the fast axes. This setup allows the derivation of full Stokes parameters.

in Figure 3. It is confirmed by Equation 3 that the configuration in Figure 4 allows the derivation of full Stokes parameters.

The green squares in Figure 4 represent the polarizers, and the arrows on them indicate the transmission axes. As previously described, the orientations of the polarizers are fixed. The orange squares are quarter-wave linear retarders, and the orientations of the fast axes shown in the figure allow the derivation of full Stokes parameters. The process of calculating them is explained. The irradiance detected at each CCD is proportional to the square of the absolute value of $\mathbf{J}_{out}$ and is given by

$$
\begin{cases}
P_{CCD1} = \mid \mathbf{LP}(0°)\,\mathbf{LR}(\lambda/4, 0°)\,\mathbf{J}_{in} \mid^2 \\[2mm]
P_{CCD2} = \mid \mathbf{LP}(45°)\,\mathbf{LR}(\lambda/4, 45°)\,\mathbf{J}_{in} \mid^2 \\[2mm]
P_{CCD3} = \mid \mathbf{LP}(90°)\,\mathbf{LR}(\lambda/4, 45°)\,\mathbf{J}_{in} \mid^2 \\[2mm]
P_{CCD4} = \mid \mathbf{LP}(135°)\,\mathbf{LR}(\lambda/4, 0°)\,\mathbf{J}_{in} \mid^2
\end{cases}
\tag{4}
$$

After computing Equation 4, full Stokes parameters can be derived from the following equations.

$$\begin{pmatrix} S_0 \\ S_1 \\ S_2 \\ S_3 \end{pmatrix} = \begin{pmatrix} P_{CCD3} + P_{CCD4} \\ 2P_{CCD1} - S_0 \\ 2P_{CCD2} - S_0 \\ P_{CCD3} - P_{CCD4} \end{pmatrix} \tag{5}$$

Since birefringence can be calculated from Stokes parameters [11], WPA-100 generates a 2D birefringence distribution.

3   Analysis (Image Science)

3.1   Reconstruction from tomographic polarimetry

3.1.1   Jones calculus Our approach to reconstructing the 3D birefringence distribution is a closed-form forward model that linearly relates polarization measurements to line projections through a discrete arrangement of index ellipsoids. The tomographic polarization measurement model for one projection is illustrated in Figure 5. Here, the material has an inhomogeneous birefringence distribution defined by index ellipsoids discretized by distance t_i. The green arrow indicates the direction of light propagation, and the birefringence values are determined by the cross-sectional index ellipse $\mathbf{P}_i$ defined in Section 1.1.3.

The polarization of the transmitted light can be determined by computing the Jones vector in sequence for each $\mathbf{P}_i$. This involves rotating the Jones vector to align with the major and minor axes of $\mathbf{P}_i$, and then accumulating the products of t_i and the birefringence values n_{ai} or n_{bi}, which are the respective optical path lengths (OPLs) in orthogonal phases. This calculation can be simplified using the equation $\mathbf{P}_{sum} = \sum_i \mathbf{P}_i / t_i^2$, where $\mathbf{P}_{sum}$ represents the total OPLs in phases, accounting for all directions [12]. The outgoing Jones vector is then obtained by applying the incident Jones vector to $\mathbf{P}_{sum}$, and polarimetric observations can be computed as the phase difference from the outgoing Jones vector.
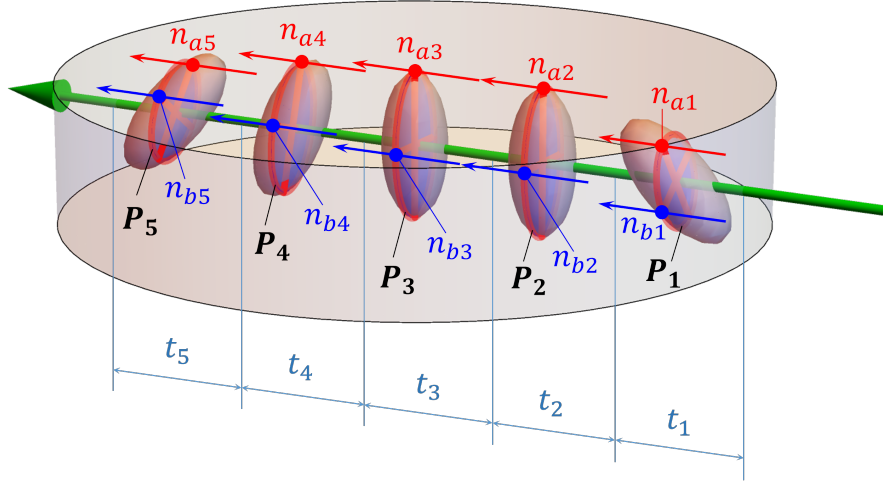
Figure 5: Light propagating through a material with an inhomogeneous birefringence distribution in the direction given by the green arrow. The birefringence values are indicated by n_{ai} and n_{bi} on the orthogonal major and minor axes, respectively. $\mathbf{P}_i$ represents cross-sectional index ellipses defined in Section 1.1.3. The index ellipsoids are discretized by distance t_i.

3.1.2 Reconstruction by pseudo-inverse

A method for reconstructing the original 3D ellipsoid from multiple cross-sectional 2D ellipses is needed. Consider the definitions

$$vec(\mathbf{A}\,\mathbf{B}\,\mathbf{C}) = (\mathbf{C} \otimes \mathbf{A}^T)^T\, vec(\mathbf{B}) \tag{6a}$$

$$\mathbf{p} = \mathbf{W}^T \mathbf{q} \tag{6b}$$

where "$\otimes$" denotes the Kronecker product, "$vec()$" denotes the vectorization operator, and $\mathbf{A}$, $\mathbf{B}$, $\mathbf{C}$ are matrices. By defining $\mathbf{W} = \mathbf{V} \otimes \mathbf{V}$, substituting $\mathbf{P}$ seen in Section 1.1.3 into Equation 6a yields Equation 6b. Here, $\mathbf{q}$ and $\mathbf{p}$ are 3^2- and 2^2-dimensional vectors, obtained by the vectorization of $\mathbf{Q}$ and $\mathbf{P}$ seen in Section 1.1.3. In addition, $\mathbf{W}$ represents a cross-sectional matrix in a different form and has $3^2 \times 2^2$ dimensions. It is noted that Equation 6b is in a linear framework and $\mathbf{p}$ represents one calculation result for one cross-sectional matrix $\mathbf{W}$. Therefore, different $\mathbf{p}$ can be obtained when different cross-sectional matrices are used. Consider $\mathbf{p}_i = \mathbf{W}_i^T \mathbf{q}$, where $\mathbf{p}_i$ represents the calculation result obtained by the ith cross-sectional matrix $\mathbf{W}_i$. By combining all k calculation results and using the pseudo-inverse
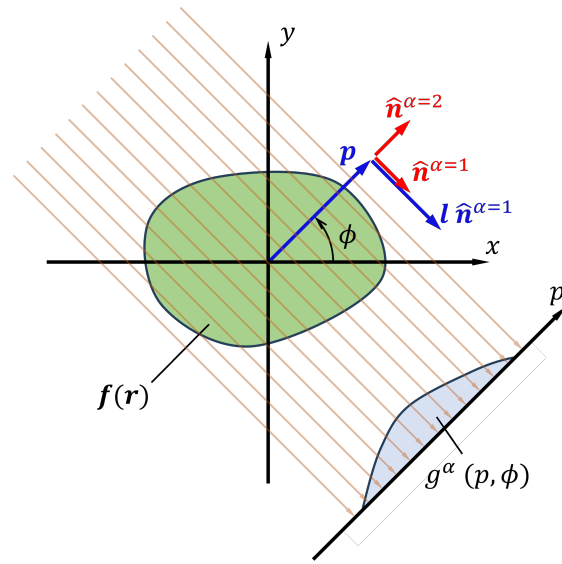
operator, the ellipsoid $\mathbf{q}$ is derived by

$$\mathbf{q} = \left(\left(\mathbf{W}_1 \cdots \mathbf{W}_k \right)^T \right)^+ \left(\mathbf{p}_1{}^T \cdots \mathbf{p}_k{}^T \right)^T \tag{7}$$

Here, the operator "+" represents the pseudo-inverse operator. Based on the above computational method, the original ellipsoid is reconstructed from the cross-sections of the ellipsoid. For a single 3D ellipsoid, the original ellipsoid can be completely reconstructed by using any three or more non-parallel cross-sectional ellipses $\mathbf{p}$. In our previous work, this algorithm has been used to reconstruct the 3D birefringence distribution of inhomogeneous and anisotropic samples [12].

3.1.3 Radon transform

The Radon transform will be introduced to enhance the versatility of reconstructing the original 3D ellipsoids. The primary challenge here is that the Radon transform is commonly applied to scalar spatial distributions, making it impossible to reconstruct 3D ellipsoids characterized by the Hermitian 3×3 matrices, as demonstrated in this study. Therefore, it is necessary to devise a Radon transform algorithm suitable for tensor fields. As a preliminary step, an algorithm that focuses on a 2D spatial distribution for a vector field instead of a tensor field is developed. This development refers to some studies related to the Radon transform for vector and tensor fields [13, 14]. Figure 6 illustrates an overview of the Radon transform for a vector field, where $\mathbf{f}(\mathbf{r})$ represents a 2D spatial distribution of

Figure 6: Overview of the Radon transform for a vector field $\mathbf{f}(\mathbf{r})$. $g^\alpha(p, \phi)$ is a 1D projection given by Equation 8. α can take a value of $\alpha = 1$ or 2. $\hat{\mathbf{n}}^{\alpha=1}$ and $\hat{\mathbf{n}}^{\alpha=2}$ represent unit vectors that are perpendicular or parallel to the direction of the vector $\mathbf{p}$. The angle ϕ denotes the direction of $\mathbf{p}$, and p is the position of the projection along $\mathbf{p}$.

the vector field, and $\mathbf{r}$ is denoted by $\mathbf{r} = (x, y)$. A 1D projection $g^{\alpha}(p, \phi)$ is obtained by a continuous set of integrals over all parallel lines in a given direction and is defined by

$$
\begin{aligned}
g^{\alpha}(p, \phi) &= \int_{\infty} d^2 r \, \hat{\mathbf{n}}^{\alpha} \, \mathbf{f}(\mathbf{r}) \, \delta(p - \mathbf{r} \, \hat{\mathbf{n}}^{\alpha=2}) \\
&= \int_{-\infty}^{\infty} dl \, \hat{\mathbf{n}}^{\alpha} \, \mathbf{f}(\mathbf{p} + l \, \hat{\mathbf{n}}^{\alpha=1})
\end{aligned}
\tag{8}
$$

Here, α can take a value of $\alpha = 1$ or 2. The 2D Radon transform is the set of 1D projections $g^{\alpha}(p, \phi)$ for all projection directions. In Equation 8, $\hat{\mathbf{n}}^{\alpha=1}$ and $\hat{\mathbf{n}}^{\alpha=2}$ represent unit vectors that are perpendicular or parallel to the direction of the vector $\mathbf{p}$, as illustrated in Figure 6. The angle ϕ denotes the direction of $\mathbf{p}$, and p is the position of the projection along $\mathbf{p}$.

Next, consider the backprojection of the vector field $\mathbf{f}(\mathbf{r})$. In Equation 8, assuming $\hat{\mathbf{n}}^{\alpha} \mathbf{f}(\mathbf{r})$ as a scalar field distribution, this equation corresponds to the ordinary Radon transform. Since the original spatial distribution can be precisely reconstructed by the filtered backprojection for the Radon transform [15], it is possible to derive the vector field in this manner. Here, noting that the relation of completeness $\sum_{\alpha=1}^{2} \hat{n}_i^{\alpha} \hat{n}_j^{\alpha} = \delta_{ij}$ (where i and j are x or y) is applied, the vector field is derived as follows.

$$
\begin{cases}
f_x(\mathbf{r}) = \int_0^{\pi} d\phi \int_{-\infty}^{\infty} d\xi \, \exp\{2\pi i \xi p\} \, |\, \xi \,| \, \{sin\phi \, G^{\alpha=1}(\xi, \phi) + cos\phi \, G^{\alpha=2}(\xi, \phi)\} \\
f_y(\mathbf{r}) = \int_0^{\pi} d\phi \int_{-\infty}^{\infty} d\xi \, \exp\{2\pi i \xi p\} \, |\, \xi \,| \, \{-cos\phi \, G^{\alpha=1}(\xi, \phi) + sin\phi \, G^{\alpha=2}(\xi, \phi)\}
\end{cases}
\tag{9}
$$

$G^{\alpha}(\xi, \phi)$ is the 1D Fourier transform of the 1D projection $g^{\alpha}(p, \phi)$ and is expressed as $G^{\alpha}(\xi, \phi) = \int_{-\infty}^{\infty} g^{\alpha}(p, \phi) \exp\{-2\pi i \xi p\} dp$. In our research, it has been verified that the vector field can be accurately reconstructed using Equation 9, thus proving that the Radon transform is also effective for vector fields.

It is anticipated that the Radon transform for tensor fields can be derived in a similar manner. Once these validations are established, the developed algorithm will be employed to reconstruct the spatial distribution of 3D ellipsoids as required in this research.

References

[1] M. Nakada, M. Saitoh, K. Toki, and H. Gokan. Change in birefringence in polycarbonate substrates under operating environments. 26:95. Publisher: IOP Publishing.

[2] A. Iwasawa and N. Funakoshi. Birefringence analysis of injection-molded polycarbonate (pc) substrates. In K. L. Mittal, editor, *Polymers in Information Storage Technology*, pages 207–215. Springer US.

[3] Photonic lattice, inc. https://www.photonic-lattice.com/en/.

[4] Masud Mansuripur. *Field, Force, Energy and Momentum in Classical Electrodynamics (Revised Edition)*. Bentham Science Publishers. Google-Books-ID: nM02DwAAQBAJ.

[5] Ariel Lipson, Stephen G. Lipson, and Henry Lipson. Optical physics. ISBN: 9780511763120 Publisher: Cambridge University Press.

[6] Russell A. Chipman, Wai-Sze Tiffany Lam, and Garam Young. *Polarized Light and Optical Systems*. CRC Press.

[7] W. C. Karl, G. C. Verghese, and A. S. Willsky. Reconstructing ellipsoids from projections. 56(2):124–139.

[8] Rita Noumeir. Detecting three-dimensional rotation of an ellipsoid from its orthographic projections. 20(6):585–590.

[9] Andrew D. Nurse. Full-field automated photoelasticity by use of a three-wavelength approach to phase stepping. 36(23):5781–5786. Publisher: Optica Publishing Group.

[10] T. Kihara. An arctangent unwrapping technique of photoelasticity using linearly polarized light at three wavelengths. 39(2):65–71. _eprint: https://onlinelibrary.wiley.com/doi/pdf/10.1046/j.1475-1305.2003.00055.x.

[11] Po-Chun Chen, Yu-Lung Lo, Tsung-Chih Yu, Jing-Fung Lin, and Tsung-Tse Yang. Measurement of linear birefringence and diattenuation properties of optical samples using polarimeter and stokes parameters. 17(18):15860–15884. Publisher: Optica Publishing Group.

[12] Masafumi Seigo, Hidetoshi Fukui, Shogo Kawano, and Meredith Kupinski. Developing a reconstruction algorithm for 3d birefringence from tomographic polarimetry. In *Polarization Science and Remote Sensing XI*, volume 12690, pages 117–127. SPIE.

[13] Michel Defrise and Grant T. Gullberg. 3d reconstruction of tensors and vectors.

[14] V. A. Sharafutdinov. *Integral Geometry of Tensor Fields.* De Gruyter.

[15] Harrison H. Barrett and Kyle J. Myers. *Foundations of Image Science.* John Wiley & Sons, Incorporated.